The atomic structure of imogolite nanotubes: A 50 years old issue reinvestigated by X-ray scattering experiments and molecular dynamics simulations

Arianna d'Angelo, Erwan Paineau, Stéphan Rouzière, Érik Elkaim, Claire Goldmann, Damien Toquer, Stéphane Rols, Pascale Launois

Graphical Abstract

The atomic structure of imogolite nanotubes: a 50 years old issue reinvestigated by X-ray scattering experiments and Molecular Dynamics simulations

Arianna D'Angelo, Erwan Paineau, Stéphan Rouzière, Érik Elkaim, Claire Goldmann, Damien Toquer, Stéphane Rols, Pascale Launois

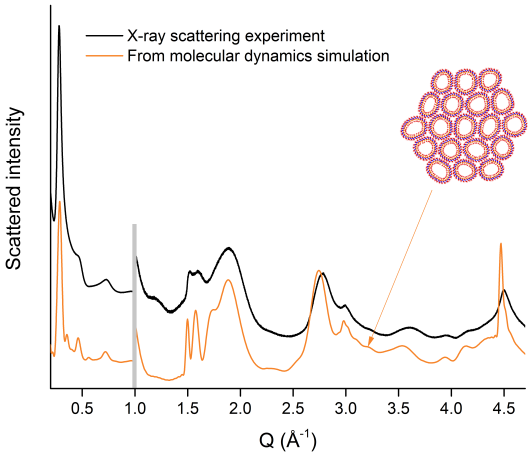

Highlights

The atomic structure of imogolite nanotubes: a 50 years old issue reinvestigated by X-ray scattering experiments and Molecular Dynamics simulations

Arianna D'Angelo, Erwan Paineau, Stéphan Rouzière, Érik Elkaim, Claire Goldmann, Damien Toquer, Stéphane Rols, Pascale Launois

- The atomic structure of synthetic imogolite nanotubes is revisited.
- X-ray scattering experiments are coupled to molecular dynamic simulations.
- Nanotubes with $N = 13$ or 14, N being the number of SiO_4 units along a circumference, are identified.
- Deformations of tubes in bundles must be taken into account in the analysis of the X-ray scattering diagrams.

The atomic structure of imogolite nanotubes: a 50 years old issue reinvestigated by X-ray scattering experiments and Molecular Dynamics simulations

Arianna D'Angelo[a,b], Erwan Paineau[a,*], Stéphan Rouzière[a], Érik Elkaim[c], Claire Goldmann[a], Damien Toquer[a], Stéphane Rols[b,*], Pascale Launois[a,*]

[a] *Université Paris Saclay, CNRS, Laboratoire de Physique des Solides, 1 rue Nicolas Appert, Orsay, 91405, France*
[b] *Institut Laue Langevin, 71 avenue des Martyrs, Grenoble, 38042, France*
[c] *Synchrotron SOLEIL, L'Orme des Merisiers, Saint-Aubin, 91190, France*

Abstract

Imogolites are clay nanotubes consisting of a curved di-octahedral gibbsite-like layer $[(OH)_3AlO_3]$ and of isolated $(OH)SiO_3$ tetrahedra connected by three mutual oxygen atoms to the octahedra, with N silicon tetrahedra along a circumference. There is a consensus that synthetic imogolites have a larger N value than natural ones, which may depend on the method of synthesis. However, N values reported in the literature over the last fifty years are given as uncertain or are not consistent. In this work, we reinvestigate the structure of synthetic imogolite nanotubes for which a value of $N = 12$ was reported. We perform X-ray scattering experiments on nanotubes in suspension and on the same sample as a dry powder after removing water. The analysis of diffractograms is based on Molecular Dynamics simulations allowing us to

*Corresponding authors
Email addresses: erwan-nicolas.paineau@universite-paris-saclay.fr (Erwan Paineau), rols@ill.fr (Stéphane Rols), pascale.launois@universite-paris-saclay.fr (Pascale Launois)

obtain imogolite nanotubes with different N values. We find that the sample is made of a mixture of nanotubes with $N = 13$ and $N = 14$. Our study points towards strong deformation of the nanotubes, assembled in bundles, in their dry state, which has to be taken into account in the analysis of measured diffractograms.

Keywords: imogolite, nanotube, structure, X-ray scattering, Molecular Dynamics simulations

---

1. Introduction

Fine fibrous aluminosilicate clay particles, named imogolite, were first reported in 1962 in Japan (Yoshinaga and Aomine, 1962). Since then, they have been found worldwide as a recurrent component in soils developed from volcanic ash or in weathered pyroclastic deposits. Despite many studies, their structure remained a mystery during the ten years following their discovery. The first structural models involved paracrystalline order and various chains of AlO_6 octahedra linked sideway by SiO_4 tetrahedra (Wada, 1967; Wada and Yoshinaga, 1969; Russel et al., 1969). An important milestone was the determination of the morphology of an imogolite fiber by high resolution electron microscopy in 1970 (Wada et al., 1970). The fibre unit observed in micrographs corresponds to a hollow tube with an inner diameter of $0.7-1$ nm and an outer diameter of $1.7 - 2.1$ nm (Wada et al., 1970). Two years later, Cradwick et al. (1972) proposed a structural model accounting for this tubular shape in an article which is still a must-read. The nominal composition of imogolite nanotubes (INT) is established to be $Al_2SiO_7H_4$. An imogolite nanotube consists of a curved di-octahedral gibbsite-like layer

[AlO_6] and of isolated SiO_4 tetrahedra connected by three mutual oxygen atoms to the octahedra (Fig. 1(a)), with the apex of the tetrahedra pointing inside the nanotube (Fig. 1(b)). H atoms are bounded to O atoms on outer and inner surfaces. The nanotube's point group is C_{2Nh} and it is periodic along its long axis with a period $T \approx 8.4$ Å (Fig. 1(c)). Equivalently with the formalism used to describe carbon nanotubes, INTs can be characterized by a chiral vector $(N, 0)$[1] (Guimarães et al., 2007; Monet et al., 2018). N is the number of SiO_4 tetrahedra on a circumference, as shown in Fig. 1(b).

A drawback of natural imogolites is that they do not form large deposits compared to other clay minerals, implying their separation from parent materials. By working on the formation conditions of INTs in the environment, Farmer et al. (1977) were the first to propose a synthesis protocol for imogolite. Their approach consisted in hydrolyzing a dilute solution of aluminum chloride and monomeric orthosilic acid in presence of sodium hydroxide, followed by an acidification step to adjust the pH below 5. This suspension was heated during almost five days. Modulations of the synthesis conditions were further reported by the same group two years later (Farmer and Fraser, 1979). They varied the precursors ratios, changed the anion species of the Al inorganic salt (ClO_4^-, NO_3^- or Cl^-, used salt-free solutions of organic precursors (ASB: aluminum-tri-*sec*-butoxide and TEOS: tetraethoxysilane).

[1]Each atomic corona is achiral, i.e. it is superimposable on itself after a mirror operation, the mirror plane containing the axis of the tube, as it is the case for $(N, 0)$ single-walled carbon nanotubes. But atomic corona cannot be in phase one with the other because of their different radii. One cannot superimpose their individual mirror planes and, interestingly, the whole nanotube structure is chiral.

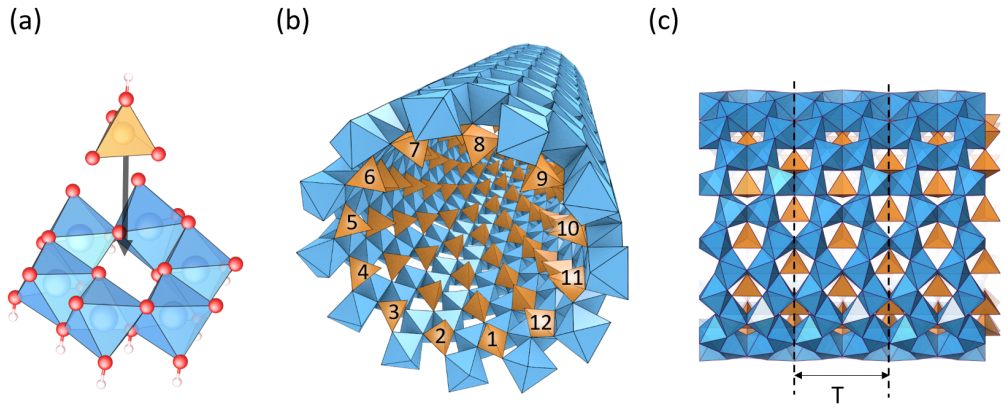

Figure 1: (a) Local view of the di-octahedral gibbsite-like layer and of the location of an SiO_4 tetrahedron, being the AlO_6 octahedra being in blue and the SiO_4 tetrahedron in orange; oxygen atoms are in red and hydrogen ones are white; (b) three-dimensional representation of a $N = 12$ nanotube; (c) side-view of the nanotube, evidencing its period T.

The optimum temperature of synthesis was found around 100°C. Since then, most of the studies were generally based on one or the other of these protocols (inorganic or organic route) with marginal changes. However, we should not overlook the remarkable study conducted by Shin-ichiro Wada, who investigated over a period of seven years the synthesis of imogolite at room temperature in conditions similar to their formation in natural environment (Wada, 1987).

Both natural and synthetic imogolite nanotubes are found to be rather monodisperse in diameter. The outer diameter of INTs is classically deduced from observations by transmission electron microscopy (TEM) (Wada et al., 1970, 1972, 1979; Wada, 1987; Koenderink et al., 1999; Bursill et al., 2000; Mukherjee et al., 2005) or from the intertube distance determined by electron

diffraction or X-ray scattering (XRS) (Cradwick et al., 1972; Barrett et al., 1991; Yang and Su, 2007; Bonelli et al., 2009; Kang et al., 2010; Thill et al., 2012; Hongo et al., 2013; Lee et al., 2014; Amara et al., 2015; Du et al., 2017; Liao et al., 2018). We shall discuss later the drawbacks of determining the intertube distance from the position of the first diffraction peak. A review of the literature over the past 50 years shows an overall increase in outer diameter and in intertube distance for synthetic INTs compared to natural ones, except for the ones synthesized at room temperature (Table S1). The nature of the anions seems to allow a modification of the diameter (Yucelen et al., 2012).The diameter values obtained from different references appear coherent for natural INTs and for INTs synthesized with $Si(OH)_4/AlCl_3/NaOH$ precursors. Some discrepancies on the reported diameters are evidenced for nanotubes synthesized using $TEOS/AlCl_3/NaOH$ and $TEOS/ASB/HClO_4$ precursors, which are most likely related to the limit of the experimental measurements or to biases in some analyses.

The diameter values are directly related to the number N of silicon atoms along a circumference (Fig. 1(b)). Numerical simulations calculate a well-defined minimum of energy as a function of the number N of silicon atoms along the nanotube circumference. However, these simulations cannot be used to predict the value(s) of N since they are performed in vacuum and do not take into account the interactions between the nanotube and its synthesis environment. Very few articles dealt with the determination of N, i.e. the determination of the atomic structure of the nanotube, either for natural and synthetic INTs. Their conclusions are reported in Table 1. It will be discussed in more details in section 3.5. However, both uncertainty in N

values for a given type of nanotube and discrepancies between N values for the same type of nanotube are already evident in Table 1.

Table 1: Value of the integer N defining the number of silicon atoms along a circumference for natural and synthetic nanotubes, as deduced from the analysis of electron diffraction (in blue) or X-ray scattering (in black) experiments. TEOS: Tetraethoxysilane; ASB: Aluminum-tri-*sec*-butoxide.

Type	Synthetic precursors	N value	Ref.
Natural	-	10 or 11 or 12	Cradwick et al. (1972)
	-	10 or 11	Alvarez-Ramírez (2007)
Synthetic	$TEOS/AlCl_3/NaOH$	12	Alvarez-Ramírez (2007)
	$TEOS/ASB/HClO_4$	12 or 14	Kang et al. (2010)
	$Na_4SiO_4/AlCl_3/NaOH$	13	Alvarez-Ramírez (2007)
		10 or 12	Guimarães et al. (2007)

After this review of the structural studies of imogolite nanotubes over the last fifty years, it appears that little progress has been made since the seminal article of Cradwick et al. (1972). Natural and synthetic INTs have the same point group C_{2Nh} and nominal composition ($Al_2SiO_7H_4$), but the values of the integer N, which defines their structures, have not been unambiguously determined. In this framework, we re-investigate the structure of synthetic INTs ($TEOS/AlCl_3/NaOH$), for which external diameters ranging from 2.2 to 3.2 nm were reported, together with a value of N equal to 12 (see Tables 1 and S1). We propose a complete X-ray scattering (XRS) study, combining laboratory and synchrotron radiation experiments on nanotubes either in suspension or in dry powder. The analysis of XRS diagrams is based on Molecular Dynamics (MD) simulations performed to obtain ther-

malized INTs with different values of N. The calculated XRS diagrams are compared to the experimental ones. We find that the sample is made of a mixture of nanotubes with $N = 13$ and $N = 14$. Our analysis points towards strong deformation of the nanotubes in their dry state, which makes the analysis of XRS diagrams tricky. Finally, previous XRS investigations from the literature are discussed in the perspective of our results.

2. Material and methods

2.1. Sample preparation and characterization

Imogolite nanotubes were synthesized from a solution of TEOS with $AlCl_3.6H_2O$ and NaOH as detailed in Belorizky et al. (2010). After hydrothermal synthesis, the suspension was purified by diafiltration with ultrapure water and concentrated by ultrafiltration. A part of the original purified suspension was kept for determining the morphology of the nanotubes by transmission electron microscopy (TEM). A highly dilute dispersion of imogolite nanotubes was prepared at 1 $mg.mL^{-1}$ in ethanol and then a drop was laid on a carbon-coated copper grid. TEM observations were made using a JEOL1400 microscope from Imagerie-Gif core facility, operated at 120 kV. The length and diameter distributions were determined using the Fiji software (Schindelin et al. (2012)). The rest of the suspension was dried in an oven at 60°C. The resulting thin film was crushed and sieved (100 μm mesh size) in order to obtain a fine powder. Based on thermogravimetric analysis (TGA) - see S.I. and figure S1, the dried powder used for XRS measurements was heated at 200°C for 2 hours.

2.2. X-ray scattering experiments

Measurement on the liquid suspension was carried out on an X-ray source produced by a Cu rotating anode (MORPHEUS platform, Laboratoire de Physique des Solides). The beam was collimated and monochromatized by parabolic confocal W/Si multilayers mirrors (Osmic), providing a 0.6 mm^2 beam at a wavelength of $\lambda = 1.5418$ Å. The INT suspension was held in a borosilicate glass capillary of 1 mm diameter (WJM-Glas, Müller GmbH, Germany). A two-dimensional diffraction pattern was acquired on a MAR detector with 150 μm pixel size, the sample to detector distance being fixed to 300 mm. The scattered intensity as a function of the wavevector Q was obtained by angular integration of the two-dimensional pattern. Geometric and polarization corrections together with correction for air adsorption between the sample and the detector were applied to the data.

Dehydrated imogolite nanotubes were obtained by heating at 200°C during 2h a powder held in a borosilicate glass capillary (diameter 0.7 mm). The capillary was flame-sealed immediately after hot removal from the oven to avoid any water adsorption from atmospheric air. X-ray scattering data were collected at the SOLEIL synchrotron, on the CRISTAL beamline using the 2-circle powder diffractometer equipped with 9 silicon-strip detectors (Mythen2 , Dectris Ltd). The monochromatic X-ray beam with a wavelength of $\lambda = 0.7287$ Å was extracted from the U20 ondulator beam by means of a Si (111) double monochromator. Synchrotron radiation is linearly polarized in the plane of the storage ring, so no polarization correction is required for measurements carried out in the vertical plane as it is the case with the 2-circle goniometer on CRISTAL beamline.

2.3. Molecular dynamics simulations

The first simulated system consists of isolated nanotubes, having $N = 13$ or 14 Si atoms along their circumference and composed of eleven unit cells along the nanotube axis z, with periodic boundary conditions applied along all dimensions of the simulation box. The period T along the long axis z is fixed to 8.45 Å, to account for the experimental XRS data. Molecular dynamics (MD) simulations were performed with the LAMMPS code (Plimpton (1995)), using a version of the CLAYFF force field (Cygan et al. (2004)) integrating the recent improvements proposed for imogolite nanotubes (Scalfi et al. (2018)), further refereed to as the *extended CLAYFF* force field (eCLAYFF). Coulomb interactions were handled with a solver that performs Ewald summation in k-space, the accuracy being equal to 10^{-5}; the cut-off distance of the Lennard-Jones potential was chosen equal to 8.5Å in order to avoid an atom to be in interaction with itself. The CLAYFF forcefield is widely used in the literature when one is concerned with clay-like materials. In a recent article, Cygan et al. (2021) reviewed its success in predicting properties of bulk nanoporous materials and their interfaces ; an entire paragraph is devoted to nanoporous materials with channels-like geometries and in particular to imogolite. The minimum energy state of our models was found by first performing an energy minimization at $T = 0$ K, using the Polak-Ribiere version of the conjugate gradient (CG) algorithm (until the net forces in the model is lower than 10^{-7} kcal/(mol.Å)). Minimization was followed by a 10 ps long NVT simulation at 300 K, using a Nosé-Hoover thermostat, with timestep 0.5 fs.

In a second step, in order to study the bundling of tubes, three different

bundles made of 19 tubes were built by MD: two with INTs having $N = 13$ or $N = 14$ and one with a mix of 10 tubes having $N = 14$ and 9 tubes having $N = 13$. The bundle with $N = 14$ INTs was obtained by packing the nanotubes organized on a two-dimensional (2D) hexagonal lattice with a lattice parameter $d = 27$ Å (26.5 Å for $N = 13$) and re-minimizing the energy of the entire bundle, considering only one unit cell along the z axis to minimize calculation time. The mixed bundle was obtained by positioning, at the lattice sites (lattice parameter $d = 27$ Å), tubes having either $N = 13$ or $N = 14$ depending on the extraction of a random number. The three bundles were first minimized at 0 K. The resulting models contain bundles of parallel tubes having a compact arrangement and an almost perfect circular cross section. With a view to studying the influence of the deviation of the tubes' cross section from this perfect circular case on the diffraction diagram, we introduced an anisotropic distribution of deformations around the tubes' surface inside the bundles. This was done by adding a layer of water – 4 to 5 wt% in mass – at different positions around the bundle and further by raising the temperature to 500 K for 10 ps, so that (i) shape deformation modes can be thermally activated and (ii) the water molecules can exert random and inhomogeneous forces on the tubes. In a final step, all the water molecules were removed from the models and the bundle was further equilibrated at 300 K for 10 ps (we have checked that the equilibrium is reached at 10 ps: the temperature of the system is found to be between 290 and 310 K after 1 ps). This operation worked perfectly: the bundles obtained this way are formed by a set of tubes with significant -but realistic and energy viable- radial deformations. The calculation of the XRS diagrams from the results

of the MD simulations is detailed in Appendix section. LAMMPS files with atomic positions of undeformed nanotubes ($N = 13$ and 14) and with atomic positions for bundles of deformed nanotubes (19 $N = 13$ tubes, 19 $N = 14$ tubes, 9 $N = 13$ tubes and 10 $N = 14$ tubes) can be uploaded from the github repository https://github.com/rolsstef/StructureLammpsFiles.

3. Results and discussion

3.1. Length and diameter distributions

The morphology of individual nanotubes is determined from transmission electron microscopy images. (Fig. 2(a)). The corresponding length distribution is presented in Fig.2(b). It displays a log-normal shape with a mean value around 290 nm, such a shape having already been reported in the literature (Yang et al., 2008; Yucelen et al., 2013). We also attempted to determine the nanotube diameter from TEM observations. The resulting distribution is reported in Fig. 2(c). The measured INT diameters are mostly in the 2.4-2.8 nm range. The error bar on diameter determination is at least ± 0.1 nm. It can thus be inferred that INTs diameters are in between 2.5 and 2.7 nm.

3.2. Comparison between X-ray scattering diagrams of an INTs suspension and of a dry powder

The XRS diagrams of synthetic imogolite nanotubes in suspension and of the resulting dry powder for wave-vectors Q smaller than 1 Å^{-1} are reported in Fig.3(a). The diagram of the suspension presents broad modulations due to the nanometric lateral extent of the nanotubes. This scattering diagram is, in first approximation, proportional to the square of the modulus of the

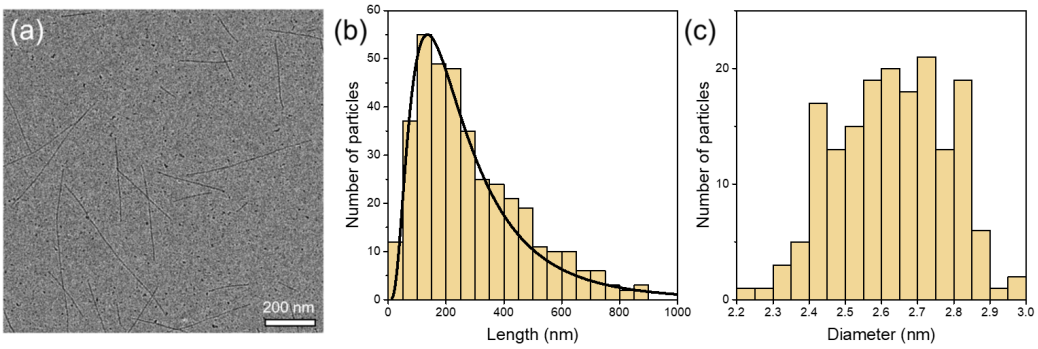

Figure 2: (a) Representative TEM image of Si-INTs and corresponding histograms of the nanotubes (b) length distribution (curve: log-normal fitting) and (c) diameter distribution.

form factor of a single tube (see Section S3 in Supplementary data). In the dry state, narrower peaks are observed in Fig.3(a) due to the assembly of INTs into bundles (Fig. S3). In the hypothesis that nanotubes hold the same shape after drying, the powder scattering diagram is the product of the squared form factor and of a structure factor for wave-vectors smaller than 1 Å^{-1} (see section S4 in Supplementary data). The zeros of the form factor should thus give minima in the powder scattering diagram. However, this is not the case for the minimum at $Q = 0.514$ Å^{-1} (Fig. 3(a)). This feature suggests that imogolite nanotubes undergo radial deformations when they self-assemble into bundles.

3.3. Wide-angle X-ray scattering: nanotube period and coherence length

Fig. 3(b) presents the powder wide-angle X-ray scattering (WAXS) diagram, for Q greater than 1 Å^{-1}. As discussed in the Appendix, the tubes are not coherent in z-position within a bundle, so that at large wave-vectors, the intensity is proportional to the angular average of the square of the modulus

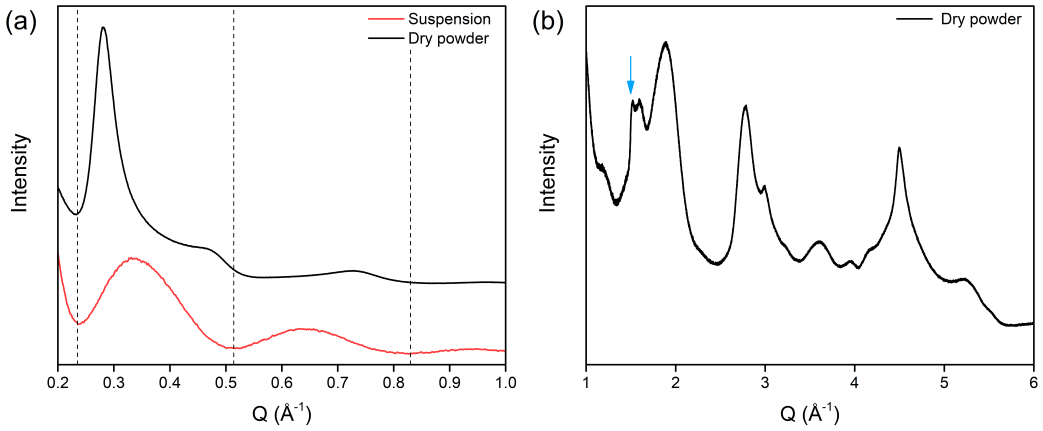

Figure 3: XRS diagrams of an INTs suspension (red) and of a powder (black) for wavevectors Q (a) smaller than 1 Å^{-1} and (b) above 1 Å^{-1}. Vertical lines in (a) locate the minima of the suspension XRS diagram. Curves are translated for the sake of clarity. The blue arrow in (b) points to $Q = 4\pi/T$ where T is the period of the nanotubes along their long axis.

of the form factor of a single nanotube. The asymmetric peak highlighted by the blue arrow in Fig. 3(b) can be used to determine the period of the INTs along their long axis (see Monet et al. (2018) and references therein). In brief, diffraction by any nanotube with a period T along its long axis z gives diffuse scattering intensity located in planes at $Q_z = l\frac{2\pi}{T}$, with l integer. When the scattered intensity is non-zero at the wave-vector $\vec{Q} = (0, 0, l\frac{2\pi}{T})$, angular powder average gives abrupt sawtooth peaks at $Q_z = l\frac{2\pi}{T}$ (Warren, 1941). For nanotubes of finite coherence length, these peaks are smoothed and the period value can be derived by determining the position of the inflexion point of its rising edge (Fig.S4). In our case, the rising edge observed in Fig. 3(b) corresponds to the 002 peak with a period T equal to 8.4 Å.

The 002 peak can also be used to determine the coherence length along

the nanotube axis (Monet et al., 2018). Comparison with calculated XRS diagrams for a powder of tubes ($N = 14$) obtained by MD simulations shows that the coherence length along the nanotube axis is of about 200 Å (see Section S5 and Fig. S4). This value is 15 times shorter than the average tube length determined from TEM observations. This small coherence length should be attributed to the occurrence of defects. Yucelen et al. (2012) evidenced different types of defects at the atomic scale in INTs, most of them involving Al vacancies. The skeleton of the nanotube being its AlO_6 dioctahedral layer, which is the locus of instabilities and constraints, the coherence length can be strongly reduced with respect to the nanotube length. The growth of INTs is based on several ingredients, with the formation of amorphous precursors and/or of curved proto-imogolite tiles, the incorporation of precursors or of proto-imogolites at the growing ends and the self-assembly of already formed nanotubes by an oriented attachment process (Yang et al., 2008; Yucelen et al., 2013; Du et al., 2017). Interestingly, Yucelen et al. (2013) evidenced that the minimum nanotube length that can form is around 20 nm, a value close to the measured coherence length. It is therefore tempting to hypothesize that the reduced coherence length along nanotubes axes could be attributed to the process of oriented attachment between a growing nanotube and a short one, with the appearance of defects within the attachment section. To confirm this conclusion, it would be interesting to compare the true length and the coherence length of natural nanotubes, which form over a much longer time frame.

3.4. Analysis of XRS diagrams from MD simulations

3.4.1. Determination of the values of N

We first compare the experimental diffractogram of the suspension with the XRS diagram of powder of single nanotubes obtained for $N = 13$ and $N = 14$ INTs (Fig. 4(a)). The minima of the $N = 14$ diagram are located at slightly larger wave-vectors than those deduced from the experimental diagram while those of the $N = 13$ INTs diagram are found at slightly smaller wave-vectors. Linear combinations between the two calculated curves give the experimental minima positions for a mixture of 50% $N = 13$ and 50% $N = 14$ INTs. Characteristic radii of the tubes are given in Table S2. The mean diameters associated to the outer oxygen atoms of the tubes are 23.4 and 25 Å for INTs with $N = 13$ and $N = 14$, respectively. This is in agreement with our TEM results (Fig. 2), especially considering that INTs can deform and flatten when deposited on the carbon coating surface for TEM observations. The mean diameters are in the average of those reported in the literature for INTs synthesized with the same precursors (see Table S1 in Supplementary data).

3.4.2. Radial deformation of nanotubes in bundles

Having determined the N values of the nanotubes in suspension, we can now analyze the diffractogram obtained for dry samples in Fig. 4(b). Imogolite nanotubes organize in bundles, on a two-dimensional (2D) hexagonal lattice, during the drying stage. The first diffraction peak around 0.28 $Å^{-1}$ corresponds to the 10 peak of this 2D lattice. Its width is inversely proportional to the number of tubes per bundle (Paineau et al. (2017)). Considering bundles formed of $n = 19$ tubes in our calculations allows to correctly ac-

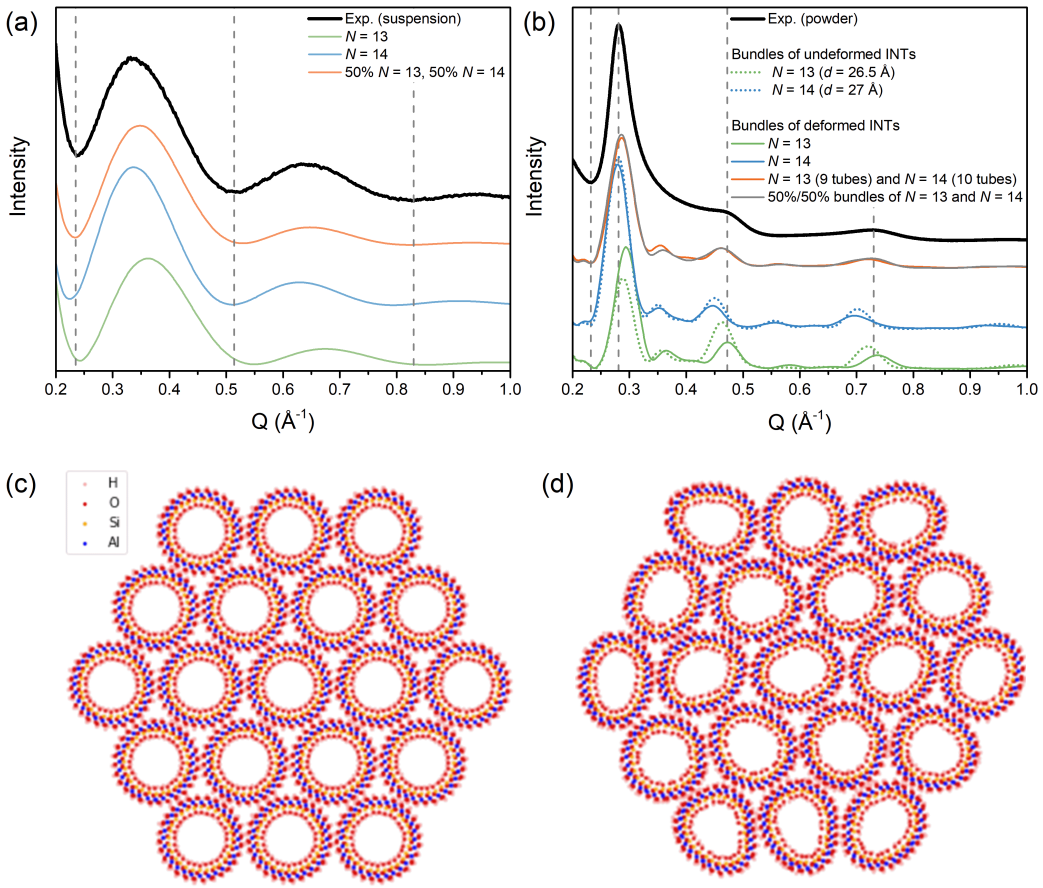

Figure 4: Comparison between calculated XRS diagrams and experimental ones obtained for (a) an INTs suspension and (b) a dry powder. Calculations are made with (1) a powder of isolated $N = 13$ INTs, $N = 14$ INTs and a mixture of 50%−50% $N = 13$ and $N = 14$ tubes; (2) powders of bundles with (i) 19 undeformed $N = 13$ tubes and of 19 undeformed $N = 14$ tubes (dotted green and blue curves, respectively); (ii) bundles of deformed tubes with 19 $N = 13$ tubes, 19 $N = 14$ tubes, a mixture of 10 $N = 14$ and 9 $N = 13$ tubes and 5O%-50% bundles with 19 deformed $N = 13$ and $N = 14$ tubes (green, blue, orange and grey curves). Vertical lines locate minima and maxima of the experimental diagrams. Curves are translated for the sake of clarity. Top view of a bundle with (c) 19 $N = 14$ undeformed INTs or (d) 19 $N = 14$ deformed INTs.

count for this width. One may however note that considering exactly $n = 19$ tubes per bundle is an approximation. The aggregation of the tubes during drying leads *a priori* to bundles of different sizes.

The undeformed tubes from MD simulations are bundled together in order to reproduce as well as possible the experimental powder diffraction pattern as illustrated in Fig. 4(c). Inter-tube distances are chosen equal to $d =$ 26.5 Å and 27 Å for $N = 13$ and $N = 14$ INTs, respectively. Calculated diagrams are shown in Fig. 4(b) as green and blue dotted curves, respectively. The calculated diagrams display similarities with the experimental one, in particular for the position of the first maximum. However, the maxima around 0.47 Å^{-1} and 0.73 Å^{-1} are too intense for $N = 13$ tubes and they are positioned at too small wave-vector values for the two calculated diagrams.

Comparison between the XRS diagrams of the suspension and of the dry powder in subsection 3.2 indicates that the nanotubes could be deformed radially when bundled. Based on MD simulations with three tubes, Tamura and Kawamura (2002) found that the central imogolite nanotube was strongly deformed. We have thus simulated bundles composed of deformed tubes, with the procedure detailed in subsection 2.3, with 19 $N = 13$ tubes, 19 $N = 14$ tubes (as shown in Fig. 4(d)) and 10 $N = 14$, 9 $N = 13$ tubes. This mixed bundle is considered because starting from a suspension with 50% $N = 13$ and 50% $N = 14$ INTs, one can expect that neighbouring tubes are combined together into bundles during the drying process whatever their N value, so that mixed bundles are formed.[2] Histograms of the lattice

[2]If one assumes that the pairing of $N = 13$ and $N = 14$ tubes is random, the probability to have a bundle with n tubes $N = 14$ and (19-n) tubes $N = 13$ is $\frac{C_{19}^{n}}{2^{19}}$.

parameter d, d being the distance between 2 nearest neighbors, and of the acute angle γ between three nearest neighbors are presented in Fig. S5. We find that $\langle\gamma\rangle = 60°$ for all bundles, so that an average hexagonal arrangement is preserved. The mean lattice parameter $\langle d\rangle$ is equal to 25.8 Å, 27.1 Å and 26.4 Å for $N = 13$, $N = 14$ and mixed bundles, respectively. The difference δ_d between the mean inter-tube distance and the mean values of the outer nanotube diameter, determined from the positions of outer hydrogens, is the same for the minimized $N = 13$ and $N = 14$ bundles (δ_d=1.1 Å).

Fig. 4(b) presents the XRS diagrams (continuous lines) calculated from simulated bundles of deformed INTs. The comparison between the dotted and the continuous lines shows that the deformation smooths the peaks above 0.4 Å^{-1}, in better agreement with the experiment. For comparison, we also report in Fig. 4b the XRS diagram for a powder of mixed bundles (9 tubes $N = 13$ and 10 tubes $N = 14$) as well as the one for a powder where half of the bundles are made with 19 deformed $N = 13$ tubes and half of them with 19 deformed $N = 14$ tubes. To quantify the deviation between the experimental and simulated curves, one minimum $Q_{mes,min}$ and three maxima $Q_{mes,max}(i)$ ($i = 1 - 3$) positions are selected (evidenced in Fig. 4(b) by vertical lines). The deviation of the simulated positions from the experimental ones are evaluated through the parameter Δ defined as

$$\Delta = \sqrt{\frac{(Q_{mes,min} - Q_{sim,min})^2}{Q_{mes,min}^2} + \sum_{i=1}^{3} \frac{(Q_{mes,max}(i) - Q_{sim,max}(i))^2}{Q_{mes,max}(i)^2}} \qquad (1)$$

The obtained Δ values for bundles of deformed INTS are 0.054, 0.074, 0.034 and 0.030 for $N = 13$, $N = 14$, the mixed bundle (9+10 tubes) and the combination of bundles with deformed $N = 13$ and $N = 14$ tubes,

respectively. The best agreements are thus obtained for the mixed bundle and for 50%-50% bundles of deformed $N = 13$ and $N = 14$ tubes.

These findings are corroborated by comparing the experimental WAXS diagram with calculated ones (Fig. 5). As stated in the Appendix, diagrams have to be calculated from the angular average of the squared form factor of individual nanotubes. Average is also taken over the nanotubes in the bundle when it is made of deformed nanotubes. Comparison between calculated diagrams for $N = 13$ (or $N = 14$) undeformed and deformed INTs shows that the radial nanotube deformation induces a smoothing of the oscillations, in better agreement with the experiment. More importantly, the WAXS diagram for mixed bundles of deformed tubes reproduce well the experimental diagram of the dry powder.

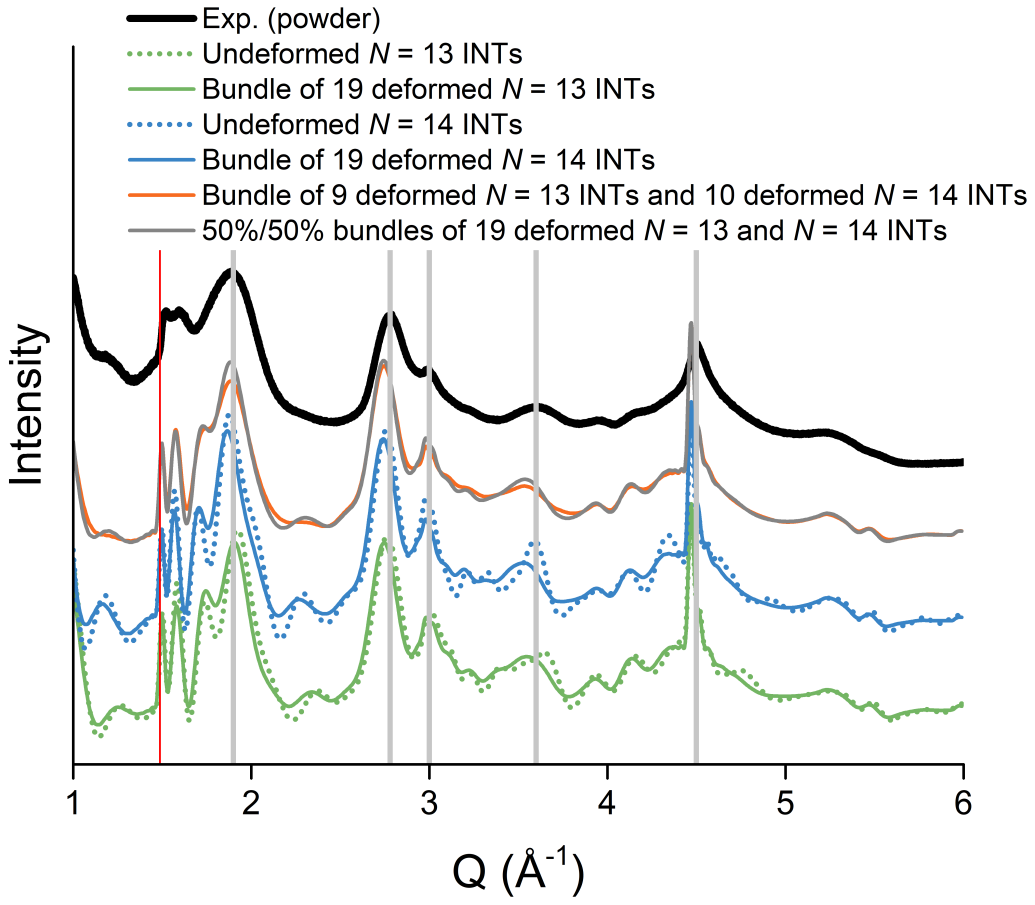

Figure 5: (a) Measured XRS diagram of an INT powder for wavevectors Q greater than 1 Å^{-1} and calculated ones for the $N = 13$ (dotted green curve) and $N = 14$ (dotted blue curve) undeformed INTs, by averaging the angularly averaged squared form factors of the nanotubes in the bundles with 19 deformed $N = 13$ INTs (continuous green curve), 19 deformed $N = 14$ INTs (continuous blue curve), 10 $N = 14$, 9 $N = 13$ deformed INTS (continuous orange curve) and by taking the average of the green and blue curves (grey curve). Vertical lines are guide for the eye. The red one gives the position of the 002 peak.

3.4.3. Robustness of the determination of $N = 13$ and $N = 14$ values

It is worth mentioning here the methodology which has been recently developed by Monet et al. (2018) to determine the structure of nanotubes of complex stoechiometry from their powder XRS diagram, by considering helicoidal symmetry and minimizing the nanotube energy using a simple semi-empirical harmonic model. This method allowed one to determine the structure of INT analogs, namely $Al_2GeO_7H_4$ nanotubes and $Al_2SiO_6CH_6$ and $Al_2GeO_6CH_6$ nanotubes (Monet et al., 2018, 2020). The determination of the structure of the $Al_2SiO_7H_4$ nanotubes studied in this article using this method is presented in section S8 in SI. The sample is found to be formed of both $N = 13$ and $N = 14$ nanotubes. The same conclusions are drawn from (i) the analysis of the suspension XRS diagram based on MD simulations with the elaborated extended CLAYFF model (Scalfi et al., 2018) and (ii) from the analysis of the powder XRS diagram with the method of Monet et al. (2018) and a simplified energetic model. The determined N values can thus be regarded with confidence. Finally, note that the limit of the simple methodology of Monet and co-workers is that it does not allow one to investigate radial deformations, which have been found to be important, because it is based on the use of the symmetry of the nanotube.

3.5. Discussion of the literature findings and analyses

We have shown that the interpretation of the powder XRS diagram of INTs is not a simple task, but that when coupled to simulations, it can bring a wealth of information. Previous analyses of electron diffraction images or powder diffraction diagrams attempting to determine the N value of $Al_2SiO_7H_4$ nanotubes are reported in Table 1. In-depth analysis of electron

diffraction data on natural INTs allowed Cradwick et al. (1972) to propose three values of $N = 10, 11$ or 12, but they could not obtain a complete interpretation of their experimental data with any N value. All other articles in Table 1 compare experimental XRS diagrams to calculated ones to obtain the N values of the studied INTs. Alvarez-Ramírez (2007) estimated the N values of three types of INTs, namely natural INTs and INTs synthesized from different precursors, the structure of the INTs being obtained by Density Functional Theory (DFT) geometry minimization. In particular, for INTs synthesized with TEOS/$AlCl_3$/NaOH precurors as the one studied here, Alvarez-Ramírez (2007) concluded that the number of silicon tetrahedra around the circumference is $N = 12$. However, the agreement between calculated and experimental XRS diagrams is not as good as what we report in Fig. 4(b) thus refuting the finding that the tubes have $N = 12$ silicon tetrahedra along their circumference. Contradictory results are also obtained for INT synthesized from Na_4SiO_4/$AlCl_3$/NaOH precursors. Alvarez-Ramírez (2007) finds that $N = 13$, while, with optimized Density Functional Tight Binding nantubes geometries, Guimarães et al. (2007) concluded to the presence of $N = 12$ nanotubes but they could not exclude $N = 10$ nanotubes. Finally, with atomic structures obtained using the CLAYFF potential, Kang et al. (2010) found $N = 12$ and/or $N = 14$ for INTs obtained with organic Si and Al precursors. Quite surprisingly, neither Guimarães et al. (2007) nor Kang et al. (2010) did consider odd values for N between the even ones they found, which would have also lead to good agreement between experiment and calculation. There is no energetic argument to avoid considering odd values. Indeed, the calculated energies per atom of an INT reported in

the literature are found to vary continuously with N (Tamura and Kawamura, 2002; Konduri et al., 2006; Guimarães et al., 2007; Zhao et al., 2009; Demichelis et al., 2010; Lee et al., 2011; González et al., 2014; Lourenco et al., 2014; Arancibia-Miranda et al., 2017; Elliott et al., 2017).

By reviewing the literature, we could see that the diameters of synthetic nanotubes are globally larger than their natural counterparts. Nevertheless, the reported values vary greatly from one study to another (Table S1), suggesting some possible experimental limitations (e.g. spatial resolution for TEM measurements) or approximations in the interpretation of the data. The purpose of this article is not to list the pros and cons between TEM, electron diffraction or X-ray scattering. However, as far as X-ray scattering is concerned, a brief historical overview of the interpretation of XRS data on INTs is instructive. By studying the growth mechanism of INTs, Mukherjee et al. (2005) revisited the indexation of the solid state packing of INTs, which was later adopted by several other authors (Lee et al., 2014; Zanzottera et al., 2012; Hongo et al., 2013). The XRS diagram analyzed in ref. Mukherjee et al. (2005) covers the Q range between 0.25 and 1.2 Å^{-1} as reproduced in Fig.S7. From the fit of the four maxima positions, indexed as 100, 110, 001 and 211, the authors deduced the following parameters for bundled aluminosilicate nanotubes: $a = b = 21.05$ Å, $c = 8.51$ Å and $\gamma = 78°$. Based on these considerations, several puzzling points need to be underlined. First, in this non-hexagonal 2D lattice, intertube distances (the distance between the center of the neighboring tubes in the plane perpendicular to their long axis z) take two values: 21.05 Å and 26.5 Å. This monoclinic arrangement should therefore imply a strong deformation of the nanotubes. In addition, the point

group of the nanotubes, C_{2N}, is such that the period projected along the tube axis is $c/2$ and not c (see Fig. 1(c)). It follows that $00l$ reflections are extincted for odd values of l, in contradiction with the 001 indexation of the third maximum of the XRS diagram. Finally, the hkl notation assumes that the tubes are organized in a coherent way in the z direction. The whole set of Bragg peak positions calculated with the 3D unit cell reported by Mukherjee et al. (2005) is shown in Fig.S8. Curiously, they have not been considered in the indexation of the four maxima but we can hardly see how they could be extincted in the experimental XRS diagram. Previous electron diffraction studies of (Farmer and Fraser, 1979; Farmer et al., 1983) showed that synthetic INTs did not form 3D crystals. This is also confirmed by the good agreement between calculations and experiments found at large Q values in this work and previous reports (Guimarães et al., 2007; Monet et al., 2018, 2020), assuming no correlations between nanotubes along z. Therefore, the indexation at small wave vectors of imogolite XRS diagrams requires only two integers hk.

This last remark allows us to discuss the crucial role of the form factor when analyzing the small wave-vector part of XRS diagrams of INT powders (Q smaller than 1 Å^{-1}). Let us consider the simple case of the undeformed tubes within hexagonal bundles with unit cell parameters $a = b = d$, d being the inter-tube distance, and $\gamma = 60°$. The scattered intensity is the product of the squared form factor modulus $|F_{INT}(Q)|^2$ and of a structure factor (see section S4 in Supplementary data). For bundles of finite size, hk Bragg peaks are enlarged while the position of their maxima is shifted with respect to the equivalent position for bundles of infinite size (Thess et al., 1996; Rols et al.,

1999; Paineau et al., 2017), as illustrated in Fig. 6(a). The position of the maxima are shifted to larger (smaller) Q values if their true position is on a rising (decreasing) edge of $\langle F^2 \rangle (Q)$ and they can be splitted into two peaks if they are located at a minimum of $\langle F^2 \rangle (Q)$. As an example, the position of the 10 peak as a function of the number of tubes in a bundle is reported in Fig. 6, together with the value of the erroneous lattice parameter which is derived from this position assuming that it is not displaced:

$$d = \frac{4\pi}{\sqrt{3}Q_{10}} \tag{2}$$

In practice, the X-ray scattering diagrams reported in the literature show broad peaks due to finite-size bundles. For 7 INTs bundles, the d position is underestimated by 2 Å. Moreover, no systematic study of the impact of deformation of tubes in bundles as a function of the number of tubes per bundle exists. In any case, it is now evident that the intertube distances reported in Table S1 should be considered with great caution as they were obtained from the position of the maximum of the first peak and from equation (2).[3]

4. Conclusions

Fifty years after the seminal article of Cradwick et al. (1972) describing the structure of imogolite nanotubes, a review of the literature reveals that the number N of silicon tetrahedra around their circumference has not been accurately determined, neither for natural nor for synthetic INTs. In

[3]In table S1, note also that Lee et al. (2014) did not use Eq. 2 and that they calculated d as equal to $\frac{2\pi}{Q_{10}}$.

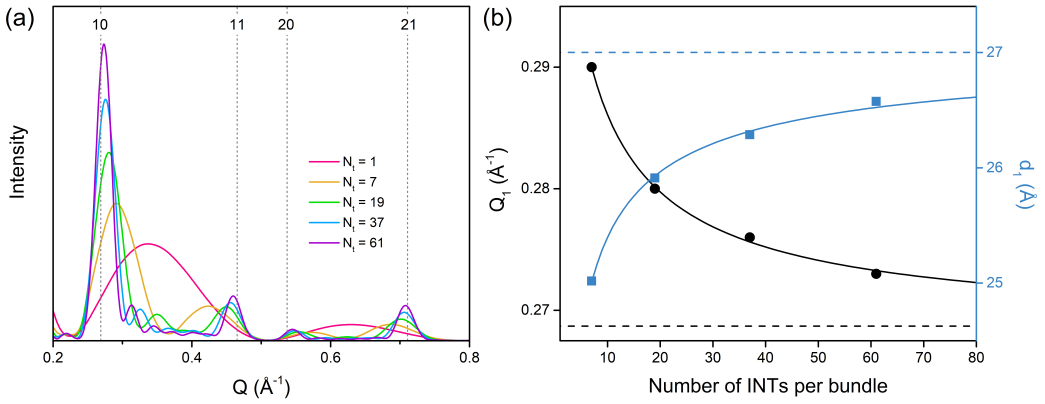

Figure 6: (a) Calculated XRS diagrams for a powder of undeformed N=14 INTs in bundles, Nt being the number of tubes per bundle. The bundle parameters are $d = 27$ Å and $\gamma = 60°$. Calculated curves are renormalized by Nt. Vertical lines give Bragg peak positions for bundles of infinite size, hk indices are noted above. (b) Position Q_1 of the first maximum of the XRS diagram (black circles) and corresponding value of the "lattice parameter" $d_1 = \frac{2\pi}{Q_1 sin(\gamma)}$ (blue squares) as a function of the number of tubes per bundle. Dashed black and blue lines give repectively the position of the 10 peak for an infinite bundle and the true lattice parameter d. Solid black and blue lines are guides to the eye.

this article, we revisited this crystallographic issue. We focused on synthetic nanotubes obtained from TEOS and $AlCl_3.H_2O$ precursors hydrolyzed with NaOH, for which it was stated that N equals 12 (Alvarez-Ramírez (2007)). The analysis of both suspension and powder XRS diagrams up to large wavevectors was carried out thanks to MD simulations based on the extended CLAYFF model. Our results show unambiguously that synthetic INTs samples are formed from both $N = 13$ and $N = 14$ nanotubes. Moreover, we highlight that the analysis of scattering diagrams is rather subtle as deformations of dry tubes assembled in bundles have to be taken into account, which had never been done before this work. It is hoped that this article can serve as a basis for re-investigating the structure of natural clay nanotubes and of synthetic analogues depending on the precursors used. Finally, the value of the coherence length along the tube axis could support a model of nanotube growth by oriented attachment.

5. CrediT authorship contribution statement

A. D'Angelo, S. Rouzière, E. Paineau, E. Elkaim, P. Launois and C. Goldmann carried out the experiments. A. D'Angelo, S. Rols and P. Launois performed XRS analysis and MD simulations. D. Toquer carried out the literature review on nanotube diameters. P. Launois, E. Paineau, A. D'Angelo and S. Rols wrote the article which was reviewed by all authors.

6. Declaration of competing interest

The authors declare that they have no known competing financial interests or personal relationships that could have appeared to influence the work

reported in this paper.

7. Acknowledgements

A. D'Angelo thanks the Institut Laue Langevin and the French ANR agency for her PhD grant (grant number ANR-18-CE09-0001, C3PO project). Synchrotron measurements on the CRISTAL beamline (SOLEIL synchrotron, Saint Aubin) were performed during BAG ЯÉCIPROCS sessions (proposals N°20191509 and 20211378).The present work has benefited from Imagerie-Gif core facility supported by l'Agence Nationale de la Recherche (ANR-11-EQPX-0029/Morphoscope; ANR-10-INBS- 04/FranceBioImaging; ANR-11-IDEX-0003-02/Saclay Plant Sciences). The authors thank P. Davidson for kindly providing the imogolite suspension, M. Jaber who performed the TGA measurement and L. Bove for interesting discussions. Figure 1 was made from pictures created by G. Monet, whom we also thank here.

8. Appendix Section: X-ray scattering calculations

Each diffractogram is calculated from the atomic positions in the last frame of a molecular dynamics trajectory. The correlation length along the tube axis z is $\sim$ 200 Å (see section 3.3), i.e. about $22T$ where T is the period along the nanotube axis. Calculations of XRS diagrams are to be made for tubes with the same length. The size of the MD simulation box along the tubes axis is equal to $11T$ for isolated nanotubes and to T for bundles. Nanotubes of correct length for XRS calculations are constructed by periodization over the box length, so that two boxes are considered for isolated INTs (translation of the first box by $11T$) and 22 boxes with nT

translations ($n = 1 - 21$) are taken for bundles of INTs. We then use the Debye formula, which allows to calculate the intensity scattered by a powder in terms of the interatomic distances:

$$I(Q) \propto \sum_{j,k} f_j(Q) f_k(Q) \frac{sin(Qd_{jk})}{Qd_{jk}} \tag{3}$$

where $f_{j(k)}(Q)$ is the atomic form factor of atom j (k) and d_{jk} is the distance between atoms j and k. Intensity calculations have been speed up using highly parallel calculation on GPUs Neverov (2017). Convolution of the calculated diagrams to the experimental resolution is useless (see section S10).

The powder constituent can be a nanotube or a bundle of nanotubes. For tubes organized in bundles, two parameters have to be considered: their relative orientations and their phasing along the z axis of the bundle. At small wave-vectors Q, when the homogeneous approximation applies, the relative orientations or translations along z of the tubes inside bundles should have no impact on the XRS diagram. We have verified this by performing calculations with tubes all having the same orientation and phasing along z and with nanotubes of random orientations and/or relative positions in z. At large Q, the orientational coherence and z-phasing between the tubes will modify the XRS diagram. In particular, without z-phasing, the intensity can be calculated by simply considering a powder of isolated tubes, i.e., by taking the coordinates of the atoms of a single tube in Eq. (3). If tubes are correlated for their z positions, their Wide Angle XRS (WAXS) diagram will present narrower modulations than for uncorrelated tubes. From this view point, the WAXS diagram of aluminosilicate nanotubes in Fig. 3(b) presents strong

similitudes with those of methylated aluminosilicate and aluminogermanate nanotubes (Monet et al., 2018) and with the one of hydroxylated aluminogermanate nanotubes (Monet et al., 2020), for which reasonable agreement between experimental and calculated diagrams was found considering isolated nanotubes. Most interestingly, Farmer and co-workers (Farmer and Fraser, 1979; Farmer et al., 1983) compared electron diffraction diagrams of natural and synthetic nanotubes. The 002 layer line presents discrete reflections for natural aluminosilicate nanotubes while it consists in a continuous streak for synthetic ones, as clearly shown in Fig.2 of ref. (Farmer et al., 1983). Natural INTs thus form three-dimensional small crystals while synthetic ones are not coherent in z-position within a bundle. This is probably due to the fact that bundles, in the case of synthetic nanotubes, are formed during the drying of their suspension, without the tubes having the option to reorganise further to minimise bundle energy.

References

Alvarez-Ramírez, F., 2007. Ab initio simulation of the structural and electronic properties of aluminosilicate and aluminogermanate natotubes with imogolite-like structure. Physical Review B 76, 125421.

Amara, M.S., Paineau, E., Rouzière, S., Guiose, B., Krapf, M.E.M., Taché, O., Launois, P., Thill, A., 2015. Hybrid, tunable-diameter, metal oxide nanotubes for trapping of organic molecules. Chemistry of Materials 27, 1488–1494.

Arancibia-Miranda, N., Escudey, M., Ramírez, R., Gonzalez, R.I., Van Duin,

A.C., Kiwi, M., 2017. Advancements in the synthesis of building block materials: experimental evidence and modeled interpretations of the effect of na and k on imogolite synthesis. The Journal of Physical Chemistry C 121, 12658–12668.

Barrett, S.M., Budd, P.M., Price, C., 1991. The synthesis and characterization of imogolite. European polymer journal 27, 609–612.

Belorizky, E., Fries, P.H., Guillermo, A., Poncelet, O., 2010. Almost ideal 1d water diffusion in imogolite nanotubes evidenced by nmr relaxometry. ChemPhysChem 11, 2021–2026.

Bonelli, B., Bottero, I., Ballarini, N., Passeri, S., Cavani, F., Garrone, E., 2009. IR spectroscopic and catalytic characterization of the acidity of imogolite-based systems. Journal of Catalysis 264, 15–30.

Bursill, L., Peng, J., Bourgeois, L., 2000. Imogolite: An aluminosilicate nanotube material. Philosophical Magazine A 80, 105–117.

Cradwick, P., Farmer, V., Russell, J., Masson, C., Wada, K., Yoshinaga, N., 1972. Imogolite, a hydrated aluminium silicate of tubular structure. Nature Physical Science 240, 187–189.

Cygan, R.T., Greathouse, J.A., Kalinichev, A.G., 2021. Advances in clayff molecular simulation of layered and nanoporous materials and their aqueous interfaces. The Journal of Physical Chemistry C 125, 17573–17589.

Cygan, R.T., Liang, J.J., Kalinichev, A.G., 2004. Molecular models of hydroxide, oxyhydroxide, and clay phases and the development of a general force field. The Journal of Physical Chemistry B 108, 1255–1266.

577 Demichelis, R., Noel, Y., d'Arco, P., Maschio, L., Orlando, R., Dovesi, R.,
578 2010. Structure and energetics of imogolite: a quantum mechanical ab
579 initio study with b3lyp hybrid functional. Journal of Materials Chemistry
580 20, 10417–10425.

581 Du, P., Yuan, P., Thill, A., Annabi-Bergaya, F., Liu, D., Wang, S., 2017.
582 Insights into the formation mechanism of imogolite from a full-range ob-
583 servation of its sol-gel growth. Applied Clay Science 150, 115–124.

584 Elliott, J.D., Poli, E., Scivetti, I., Ratcliff, L.E., Andrinopoulos, L., Dziedzic,
585 J., Hine, N.D., Mostofi, A.A., Skylaris, C.K., Haynes, P.D., et al., 2017.
586 Chemically selective alternatives to photoferroelectrics for polarization-
587 enhanced photocatalysis: The untapped potential of hybrid inorganic nan-
588 otubes. Advanced Science 4, 1600153.

589 Farmer, V., Adams, M., Fraser, A., Palmieri, F., 1983. Synthetic imogolite:
590 properties, synthesis and possible applications. clay Minerals 18, 459–472.

591 Farmer, V., Fraser, A., Tait, J., 1977. Synthesis of imogolite: a tubular
592 aluminium silicate polymer. Journal of the Chemical Society, Clinical
593 Communications 12, 462–463.

594 Farmer, V.C., Fraser, A., 1979. Synthetic imogolite, a tubular hydroxyalu-
595 minium silicate, in: Developments in Sedimentology. Elsevier. volume 27,
596 pp. 547–553.

597 González, R.I., Ramírez, R., Rogan, J., Valdivia, J.A., Munoz, F., Valencia,
598 F., Ramírez, M., Kiwi, M., 2014. Model for self-rolling of an aluminosilicate

sheet into a single-walled imogolite nanotube. The Journal of Physical Chemistry C 118, 28227–28233.

Guimarães, L., Enyashin, A.N., Frenzel, J., Heine, T., Duarte, H.A., Seifert, G., 2007. Imogolite nanotubes: stability, electronic, and mechanical properties. ACS Nano 1, 362–368.

Hongo, T., Sugiyama, J., Yamazaki, A., Yamasaki, A., 2013. Synthesis of imogolite from rice husk ash and evaluation of its acetaldehyde adsorption ability. Industrial & Engineering Chemistry Research 52, 2111–2115.

Kang, D.Y., Zang, J., Wright, E.R., McCanna, A.L., Jones, C.W., Nair, S., 2010. Dehydration, dehydroxylation, and rehydroxylation of single-walled aluminosilicate nanotubes. ACS Nano 4, 4897–4907.

Koenderink, G.H., Kluijtmans, S.G., Philipse, A.P., 1999. On the synthesis of colloidal imogolite fibers. Journal of colloid and interface science 216, 429–431.

Konduri, S., Mukherjee, S., Nair, S., 2006. Strain energy minimum and vibrational properties of single-walled aluminosilicate nanotubes. Physical Review B 74, 033401.

Lee, H., Jeon, Y., Lee, Y., Lee, S.U., Takahara, A., Sohn, D., 2014. Thermodynamic control of diameter-modulated aluminosilicate nanotubes. The Journal of Physical Chemistry C 118, 8148–8152.

Lee, S.U., Choi, Y.C., Youm, S.G., Sohn, D., 2011. Origin of the strain energy minimum in imogolite nanotubes. The Journal of Physical Chemistry C 115, 5226–5231.

Liao, Y., Picot, P., Brubach, J.B., Roy, P., Le Caër, S., Thill, A., 2018. Self-supporting thin films of imogolite and imogolite-like nanotubes for infrared spectroscopy. Applied Clay Science 164, 58–67.

Lourenco, M.P., Guimaraes, L., Da Silva, M.C., De Oliveira, C., Heine, T., Duarte, H.A., 2014. Nanotubes with well-defined structure: single-and double-walled imogolites. The Journal of Physical Chemistry C 118, 5945–5953.

Monet, G., Amara, M.S., Rouzière, S., Paineau, E., Chai, Z., Elliott, J.D., Poli, E., Liu, L.M., Teobaldi, G., Launois, P., 2018. Structural resolution of inorganic nanotubes with complex stoichiometry. Nature communications 9, 1–9.

Monet, G., Paineau, E., Chai, Z., Amara, M.S., Orecchini, A., Jimenéz-Ruiz, M., Ruiz-Caridad, A., Fine, L., Rouzière, S., Liu, L.M., et al., 2020. Solid wetting-layers in inorganic nano-reactors: the water in imogolite nanotube case. Nanoscale Advances 2, 1869–1877.

Mukherjee, S., Bartlow, V.M., Nair, S., 2005. Phenomenology of the growth of single-walled aluminosilicate and aluminogermanate nanotubes of precise dimensions. Chemistry of Materials 17, 4900–4909.

Neverov, V.S., 2017. Xansons: Gpu-accelerated simulator of diffraction patterns of nanoparticles. SoftwareX 6, 63–68.

Paineau, E., Amara, M., Monet, G., Peyre, V., Rouzière, S., Launois, P., 2017. Effect of ionic strength on the bundling of metal oxide imogolite nanotubes. J. Phys. Chem. C 121, 21740–21749.

Plimpton, S., 1995. Fast parallel algorithms for short-range molecular dynamics. Journal of computational physics 117, 1–19.

Rols, S., Almairac, R., Henrard, L., Anglaret, E., Sauvajol, J.L., 1999. Diffraction by finite-size crystalline bundles of single wall nanotubes. The European Physical Journal B-Condensed Matter and Complex Systems 10, 263–270.

Russel, J., McHardy, W., Fraser, A., 1969. Imogolite: a unique aluminosilicate. Clay Minerals 8, 87–99.

Scalfi, L., Fraux, G., Boutin, A., Coudert, F.X., 2018. Structure and dynamics of water confined in imogolite nanotubes. Langmuir 34, 6748–6756.

Schindelin, J., Arganda-Carreras, I., Frise, E., Kaynig, V., Longair, M., Pietzsch, T., Preibisch, S., Rueden, C., Saalfeld, S., Schmid, B., et al., 2012. Fiji: an open-source platform for biological-image analysis. Nature methods 9, 676–682.

Tamura, K., Kawamura, K., 2002. Molecular dynamics modeling of tubular aluminum silicate: Imogolite. The Journal of Physical Chemistry B 106, 271–278.

Thess, A., Lee, R., Nikolaev, P., Dai, H., Petit, P., Robert, J., Xu, C., Lee, Y.H., Kim, S.G., Rinzler, A.G., et al., 1996. Crystalline ropes of metallic carbon nanotubes. science 273, 483–487.

Thill, A., Guiose, B., Bacia-Verloop, M., Geertsen, V., Belloni, L., 2012. How the diameter and structure of $(OH)_3Al_2O_3Si_x\ Ge_{1-x}$ oh imogolite nan-

667 otubes are controlled by an adhesion versus curvature competition. The
668 Journal of Physical Chemistry C 116, 26841–26849.

669 Wada, K., 1967. A structural scheme of soil allophane. American Mineralo-
670 gist: Journal of Earth and Planetary Materials 52, 690–708.

671 Wada, K., Henmi, T., Yoshinaga, N.t., Patterson, S., 1972. Imogolite and
672 allophane formed in saprolite of basalt on maui, hawaii. Clays and Clay
673 Minerals 20, 375–380.

674 Wada, K., Yoshinaga, N., 1969. The structure of "imogolite". American
675 Mineralogist: Journal of Earth and Planetary Materials 54, 50–71.

676 Wada, K., Yoshinaga, N., Yotsumoto, H., Ibe, K., Aida, S., 1970. High
677 resolution electron micrographs of imogolite. Clay Minerals 8, 487–489.

678 Wada, S.i., 1987. Imogolite synthesis at 25 c. Clays and Clay Minerals 35,
679 379–384.

680 Wada, S.i., Eto, A., Wada, K., 1979. Synthetic allophane and imogolite.
681 Journal of Soil Science 30, 347–355.

682 Warren, B.E., 1941. X-ray diffraction in random layer lattices. Phys. Rev. 59,
683 693–698. URL: https://link.aps.org/doi/10.1103/PhysRev.59.693,
684 doi:10.1103/PhysRev.59.693.

685 Yang, H., Su, Z., 2007. Individual dispersion of synthetic imogolite nanotubes
686 via droplet evaporation. Chinese Science Bulletin 52, 2301–2303.

687 Yang, H., Wang, C., Su, Z., 2008. Growth mechanism of synthetic imogolite
688 nanotubes. Chemistry of Materials 20, 4484–4488.

689 Yoshinaga, N., Aomine, S., 1962. Imogolite in some ando soils. Soil Science
690 and Plant Nutrition 8, 22–29.

691 Yucelen, G.I., Kang, D.Y., Guerrero-Ferreira, R.C., Wright, E.R., Beckham,
692 H.W., Nair, S., 2012. Shaping single-walled metal oxide nanotubes from
693 precursors of controlled curvature. Nano letters 12, 827–832.

694 Yucelen, G.I., Kang, D.Y., Schmidt-Krey, I., Beckham, H.W., Nair, S., 2013.
695 A generalized kinetic model for the formation and growth of single-walled
696 metal oxide nanotubes. Chemical Engineering Science 90, 200–212.

697 Zanzottera, C., Vicente, A., Celasco, E., Fernandez, C., Garrone, E., Bonelli,
698 B., 2012. Physico-chemical properties of imogolite nanotubes function-
699 alized on both external and internal surfaces. The Journal of Physical
700 Chemistry C 116, 7499–7506.

701 Zhao, M., Xia, Y., Mei, L., 2009. Energetic minimum structures of imogolite
702 nanotubes: A first-principles prediction. The Journal of Physical Chem-
703 istry C 113, 14834–14837.